

## Article

# Carbon-in-Silicate Nanohybrid Constructed by In Situ Confined Conversion of Organics in Rectorite for Complete Removal of Dye from Water

Qingdong He <sup>†</sup>, Jie Qi <sup>†</sup>, Xiangyu Liu, Huan Zhang, Yiwen Wang, Wenbo Wang <sup>\*†</sup> and Fang Guo <sup>\*</sup>

College of Chemistry and Chemical Engineering, Inner Mongolia University, Hohhot 010021, China; 18847744604@163.com (Q.H.); jieino@163.com (J.Q.); lxy13257244737@163.com (X.L.); hzhang1989@163.com (H.Z.); wangyiwen199501@163.com (Y.W.)

<sup>\*</sup> Correspondence: wangwenbo@imu.edu.cn (W.W.); guofang@imu.edu.cn (F.G.)

<sup>†</sup> These authors contributed equally to this work.

**Abstract:** The complete removal of low concentration organic pollutants from wastewater to obtain clean water has always been a highly desired but challenging issue. In response to this, we proposed a new strategy to fabricate a carbon-in-silicate nanohybrid composite by recycling dye-loaded layered clay adsorbent and converting them to new heterogeneous carbon-in-silicate nanocomposite through an associated calcination-hydrothermal activation process. It has been confirmed that most of the dye molecules were present in waste rectorite adsorbent using an intercalation mode, which can be in situ converted to carbon in the confined interlayer spacing of rectorite. The further hydrothermal activation process may further improve the pore structure and increase surface active sites. As expected, the optimal composite shows extremely high removal rates of 99.6% and 99.5% for Methylene blue (MB) and Basic Red 14 (BR) at low concentrations (25 mg/L), respectively. In addition, the composite adsorbent also shows high removal capacity for single-component and two-component dyes in deionized water and actual water (i.e., Yellow River water, Yangtze River water, and seawater) with a removal rate higher than 99%. The adsorbent has good reusability, and the adsorption efficiency is still above 93% after five regeneration cycles. The waste clay adsorbent-derived composite adsorbent can be used as an inexpensive material for the decontamination of dyed wastewater.

**Keywords:** rectorite; adsorbent; recycling; adsorption; wastewater



**Citation:** He, Q.; Qi, J.; Liu, X.; Zhang, H.; Wang, Y.; Wang, W.; Guo, F. Carbon-in-Silicate Nanohybrid Constructed by In Situ Confined Conversion of Organics in Rectorite for Complete Removal of Dye from Water. *Nanomaterials* **2023**, *13*, 2627. <https://doi.org/10.3390/nano13192627>

Academic Editor: Alessandro Barge

Received: 31 August 2023

Revised: 17 September 2023

Accepted: 20 September 2023

Published: 23 September 2023



**Copyright:** © 2023 by the authors. Licensee MDPI, Basel, Switzerland. This article is an open access article distributed under the terms and conditions of the Creative Commons Attribution (CC BY) license (<https://creativecommons.org/licenses/by/4.0/>).

## 1. Introduction

According to statistics, more than 100 tons of dye pollutants are discharged into the water environment every year [1]. The textile industry is the largest source of water pollution, followed by the paint, paper, leather, and printing industries [2]. These toxic dye wastewaters have caused great harm to human health, organisms, and ecosystems. How to economically and effectively remove dye pollutants in wastewater has become an urgent problem that needs to be solved [3–6]. The adsorption method is preferred as one of the most hopeful approaches for removing all kinds of pollutants owing to its simplicity, high efficiency, easy operation, reusability, and low cost [7–9].

In recent years, attempts have been made to remove dyes from wastewater with different adsorbent materials, such as activated carbon [10,11], polymer materials [12–14], modified clay [15], graphene [16], MOF [17], biochar [18], copper selenides [19], magnetic NiFe layered double hydroxide decorated diatomite [20], hybrid porous hexagonal boron nitride-based magnetic aerogel [21], and others. With the increasing demand for high water purification levels, the development of new adsorbents with a high dye removal rate, strong applicability in diverse water bodies, low cost, and wide range of sources has been pursued. Silicate clay minerals have been commonly recognized as low-cost and

efficient adsorbents for the removal of pollutants due to their abundance, non-toxicity, stability, low cost, safety, and other advantages [22,23]. The clay minerals can be simply modified or compounded with other species to further elevate the adsorption capability. For example, the attapulgite/carbon composite shows an adsorption capacity (37.79 mg/g) and removal rate (95%) that is superior to raw attapulgite [24]. The magnetic magnesium-rich silicate adsorbent derived from natural attapulgite clay shows an adsorption capacity of 116.1 mg/g and 169.5 mg/g for methylene blue and cationic yellow dyes, respectively, and its performance is better than that of raw attapulgite clay [25]. The native advantages of clay minerals make them promising candidate for the development of high-performance adsorption materials.

Rectorite (R) is a unique two-dimensional layered clay mineral, which is composed of mica-like layers and montmorillonite-like layers in a ratio of 1:1 [26]. Compared with other layered clay minerals, it not only has cation exchange, water absorption, and swelling properties similar to montmorillonite, but also has high temperature-resistant properties similar to mica [27]. Rectorite is used to adsorb organic dyes in wastewater through hydrogen bond interactions, electrostatic attraction and ion exchange due to its pores, cation exchange capacity, surface negative charges, and surface silanol groups [28]. Although a series of natural clay minerals (such as rectorite) are widely used in the adsorption of dyes, the spent adsorbents will become solid waste, and its improper disposal will cause secondary pollution to the environment and a huge waste of mineral resources. Therefore, the effective disposal of the dye-adsorbed clay waste is extremely important [29], and relevant research have received much more attentions. Wang et al. synthesized a mesoporous silicate/carbon composite adsorbent from attapulgite-based waste dye adsorbent, which has a high removal capacity for tetracycline, methylene blue, and crystal violet [30]. Tian et al. use attapulgite (APT)-based dye adsorbent as a raw material to synthesize ternary attapulgite/carbon/silver nanoparticles (APT/C/AgNPs), nanocomposite with satisfactory adsorption and catalytic properties [31]. Zhai et al. converted methylene blue-adsorbed attapulgite at different temperatures to obtain a photocatalytic material with excellent efficiency for the degradation of bisphenol A [32]. These research proved a sustainable approach to convert waste to useful new materials. From previous research, it was also found that the conversion behavior of dye and the performance of the resulting adsorbent are highly dependent on the original structure of clay minerals. It is necessary to intensively examine the structure and performance of the composite derived from clay minerals with interlayered structures.

As a continuation of our systematic research work, this paper focused on the conversion and activation of waste rectorite adsorbent for production of highly efficient carbon-in-silicate adsorbent. The conversion behavior of dye in the interlayered clay was studied, the synthesis parameters were optimized, the change of microstructures of rectorite in the composites were explored. The adsorption behavior of the composite towards dyes from one-component and two-component system in different water medium was explored.

## 2. Materials and Methods

### 2.1. Materials

Rectorite (abbreviated as R) was obtained from Jingmen city, Hubei Province, China. Dye-loaded rectorite (MB-R) powder was obtained by the following process: rectorite powder and 1000 mL of MB dye solution (concentration, 5 g/L) were mixed together under continuous stirring for 24 h at room temperature to attain saturated adsorption. The solid was separated from the solution by a centrifugation process, and then crushed into a powder with a particle size < 76  $\mu\text{m}$ . Methylene blue (MB) was bought from Adamas-beta Co., Ltd. in Shanghai, China. Basic Red 14 (BR) was bought from Duly Chemical Reagent Co., Ltd. in Nanjing, China. Hydrochloric acid (HCl aqueous solution) was purchased from Beijing Innochem Chemical Reagent Co., Ltd., in Beijing, China. Yangtze River water was sourced from the Jingzhou city, China. Yellow River water is taken from the Ordos

city, China. Seawater is taken from the Bohai Sea, China (located at Tianjin, China). The parameters of the three actual water bodies are shown in Table S1 (Supplementary Material).

## 2.2. Synthesis of Carbon-in-Silicate Nanohybrid Composites

The composites were prepared via the following two-step process (Figure S1 in Supplementary Material). The first step is the carbonization process of dye-loaded rectorite. First, the MB-loaded rectorite powder (1 g) was placed in a tube furnace, and then calcined at 600 °C for 3 h under a nitrogen atmosphere (heating rate: 5 °C/min). The resultant black solid powder was marked as R/C. The second step is the activation of the R/C composite. The R/C powder (1 g) was dispersed into 20 mL of hydrochloric acid solution with different concentrations (0.5, 1, 2, 3, and 4 mol/L, respectively). The mixture was magnetically stirred for 30 min to obtain a uniform dispersion. Subsequently, the dispersion was transferred into hydrothermal reaction tank with Teflon liner (100 mL volume), then sealed and placed in an oven at 160 °C for different time intervals (2 h, 3 h, 4 h, 6 h, 8 h, and 12 h, respectively). After the hydrothermal process was completed, the reaction tank was naturally cooled to ambient temperature. The product was separated from the reaction mixture *via* a centrifugation process, washed several times with deionized water, dried, pulverized, and screened to obtain the final product. The product was labeled as R/C-xHAy (x is the amount-of-substance concentration of HCl solution, mol/L; y is the hydrothermal reaction time, h).

## 2.3. Adsorption Experiments

### 2.3.1. Adsorption Performance Test

The effects of pH, kinetics, and isotherm on adsorption experiments are detailed in the Supplementary Material.

### 2.3.2. Test for Adsorption Efficiency of R/C-2HA4h Composite

Different doses of the composite adsorbents (0.5, 1.0, 1.5, 2.0, and 3.0 g/L, respectively) were added to the aqueous solution of MB or BR dye (concentration: 25 mg/L). After the adsorption process reaches equilibrium, the UV-Visible spectrum of the dye solution was scanned, the digital photograph of the solution was taken, and the removal rate of dyes after adsorption by the adsorbent was calculated. The adsorption capacity of the composite adsorbent (dose: 0.5 g/L) towards MB or BR dyes in different water bodies (i.e., Deionized water, Yangtze River water, Yellow River water, and Seawater) (dye concentration: 200 mg/L) was evaluated according to a similar procedure. The parameters of the three actual water bodies are shown in Table S2 (Supplementary Material). The co-adsorption properties of the composite towards the mixed dye solutions of MB and BR in different water medium was evaluated. Different doses of the composites (0.5 g/L, 1.0 g/L, 1.5 g/L, 2.0 g/L, 3.0 g/L, 4.0 g/L, and 5.0 g/L, respectively) were added to 20 mL of mixed dye solution (25 mg/L for MB and BR). After adsorption, the removal rate of dye by the adsorbent was tested and calculated, the UV-Visible spectrum of the solution was scanned, and the digital photograph of the solution was taken.

## 2.4. Characterizations

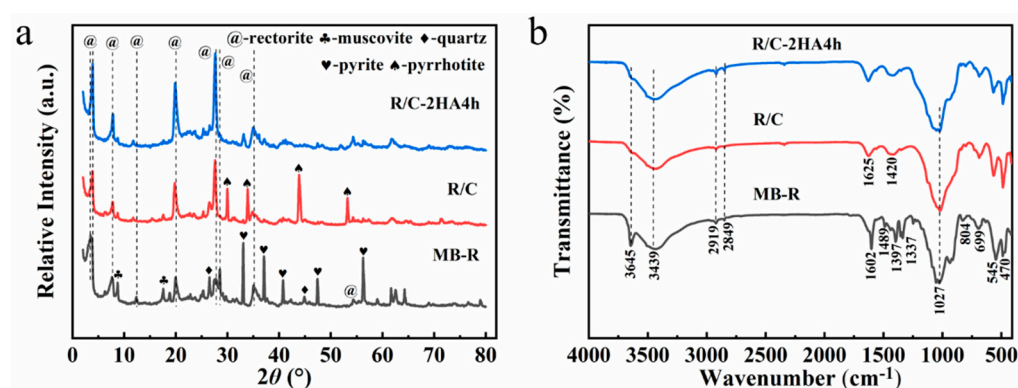
The instruments and methods used to characterize the composite adsorbents are shown in the Supplementary Material.

## 3. Results and Discussion

### 3.1. Structure and Morphology of Composites

The XRD patterns of MB-loaded rectorite and R/C and R/C-2HA4h adsorbents are shown in Figure 1. The characteristic reflections of rectorite ( $2\theta$  values: 3.48°, 7.66°, 19.94°, 27.40°, and 35.06°) [27] (JCPDS Card No. 29-1495), muscovite ( $2\theta$  values: 8.74° and 17.50°) [30], quartz ( $2\theta$  values: 26.46° and 44.84°) [25], and pyrite ( $2\theta$  values: 33.02°, 37.04°, 40.74°, 47.40°, and 56.28°) (JCPDS No. 71-0053) [33] appeared in the XRD patterns of

MB-R, which indicate that small amounts of associated minerals coexist with the rectorite mineral. After MB-R was calcined at 600 °C under nitrogen atmosphere, the diffraction peak of rectorite at  $2\theta = 3.48^\circ$  (0 0 1 plane) shifts to larger angle, which confirms that the layer spacing decreases, and the MB in the interlayer spacing of rectorite was converted to carbon [29,34]. Figure 1a and Figure S2 (Supplementary Material) exhibit the XRD patterns of R/C after activation with different concentrations of acid solution and different hydrothermal activation times. When the concentration of acid solution and hydrothermal activation time gradually increase, the intensity of the diffraction peaks of (0 0 1) and (0 0 2) crystal planes decrease significantly, which is due to the partial removal of metal ions (such as  $Mg^{2+}$ ,  $Al^{3+}$ ) on the rectorite sheet during acid activation [35] and the formation of the amorphous region. When the concentration of acid solution is 4 mol/L, the reflection peaks of the (0 0 1) and (0 0 2) crystal planes disappear, indicating the acid activation process can remove some metal ions from the rectorite layer to create active adsorption sites that are beneficial to the adsorption of dyes.



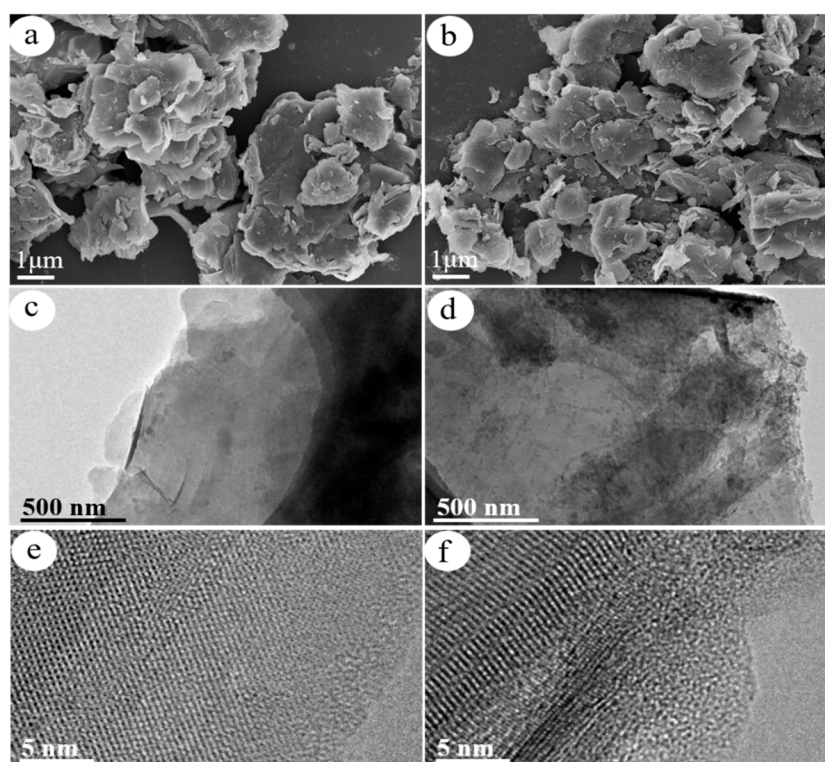
**Figure 1.** (a) XRD patterns of MB-R, R/C and R/C-2HA4h; (b) FTIR spectra of MB-R, R/C and R/C-2HA4h.

Figure 1b shows the FTIR spectra of MB-R, R/C, and R/C-2HA4h. In the FTIR spectrum of MB-R, the bands at  $3645\text{ cm}^{-1}$ ,  $3439\text{ cm}^{-1}$ , and  $1023\text{ cm}^{-1}$  are the stretching vibration of Al-OH, the stretching vibration of O-H, and the stretching vibration of Si-O-Si, respectively [27]. The bands at  $1336$ ,  $1395$ ,  $1489$ , and  $1602\text{ cm}^{-1}$  are assigned to the antisymmetric and symmetric deformation bands of  $CH_3$ , aromatic C-N, and aromatic C-C in MB, respectively [30,36,37]. The bands at  $2919\text{ cm}^{-1}$  and  $2849\text{ cm}^{-1}$  are the stretching vibration bands of C-H in  $-CH_3$  and  $-CH_2$ , respectively [38]. After calcination treatment, the absorption bands of MB disappear, but the stretching vibration band of C-H in  $-CH_3$  and  $-CH_2$  still appears at  $2917\text{ cm}^{-1}$  and  $2849\text{ cm}^{-1}$ , proving that the MB in the layer spacing of rectorite was converted to carbon after calcination. The Al-OH adsorption band at  $3641\text{ cm}^{-1}$  almost disappears after calcination, which is due to the dehydroxylation reaction in the rectorite layer during the calcination process [27].

Figure S2c,d (Supplementary Material) shows the changes of functional groups on the adsorbent after R/C was activated with different concentrations of acid solution (fixed activation time: 8 h) and hydrothermal time (fixed acid concentration: 2 mol/L). With the gradual increase of acid concentration and the extension of activation time, the absorptive bands of Al-OH at  $3641\text{ cm}^{-1}$  gradually disappeared, due to the dehydroxylation reaction of the rectorite layer [27], and the surface of rectorite was slightly etched. The stretching vibration bands of C-H in R/C at  $2917\text{ cm}^{-1}$  and  $2849\text{ cm}^{-1}$  almost disappeared after treatment with 4 mol/L of acid solution for 8 h, indicating that the high concentration of acid solution makes the carbon fall off by breaking the carbon/silicate interface.

Figure 2a,b displays the SEM images of R/C and R/C-2HA4h, respectively. Rectorite maintains its complete lamellar structure after calcination process. However, its layer structure is slightly damaged after acid activation process, and some fragments were seen on it. Figure 2c,e and Figure 2d,f display the TEM images of R/C and R/C-2HA4h,

respectively. The R/C composite still shows complete lamellar structure with uniform carbon layer (Figure 2c). After acid activation, the layer structure of rectorite is slightly damaged and the complete carbon layer is observed (Figure 2d). This is because the acid activation partially leached the metal ions (i.e.,  $Mg^{2+}$ ,  $Al^{3+}$ ) on the surface of rectorite layer, and the layer structure is slightly changed. The amorphous region caused by acid etching are observed in the high magnification TEM picture of R/C-2HA4h (Figure 2f), which is favorable to increase the adsorption sites on the surface of rectorite. The EDS elemental analysis of R/C and R/C-2HA4h (Figure S3 in Supplementary Material) also proves the change of metal ions on the surface of rectorite layer. Before and after acid activation, the Mg and Al content on the surface of R/C decreased by 7.97% and 7.30%, respectively.



**Figure 2.** SEM images of (a) R/C and (b) R/C-2HA4h; and TEM images of (c,e) R/C and (d,f) R/C-2HA4h at different magnifications.

### 3.2. Raman Spectra Analysis

Raman spectroscopy is a commonly used method to study the structural characteristics of graphitic carbonaceous materials. Raman spectra of the MB-R, RE/C, and R/C-2HA4h composites were analyzed to reveal the presence of carbon in the materials. As shown in Figure 3a, the peaks at 1628, 1573, and 1584  $cm^{-1}$  are identified as Raman shifts of G bands in MB-R, R/C, and R/C-2HA4h, respectively, which belong to the characteristic peak of graphitized carbon ( $sp^2-C$ ) [39]. The peaks at 1451, 1395, and 1392  $cm^{-1}$  are identified as the Raman shifts of the D bands in MB-R, R/C, and R/C-2HA4h, respectively, which are ascribed to the absence of ordered carbon atoms or defective carbon atoms ( $sp^3-C$ ) [39]. The intensity ratio of D-band to G-band ( $I_D/I_G$ ) can generally be used as an index to evaluate the order degree of carbon structure. The  $I_D/I_G$  values of MB-R, R/C, and R/C-2HA4h are 0.44, 0.99, and 0.99, respectively. There are many peaks in the Raman spectrum of MB-R, which is due to the existence of MB in the MB-R, which is dominated by graphitized carbon. When MB-R was converted to R/C, the  $I_D/I_G$  value was close to 1, and there were no other peaks in the Raman spectrum, accounting for the dye in MB-R being completely transformed into carbon. After the acid activation, the  $I_D/I_G$  value of R/C-2HA4h is still the same as that of R/C, but the respective peak intensities have increased, indicating that the moderate acid activation process does not change the state of the carbon species. These

results indicate that the carbon species in R/C and R/C-2HA4h are graphitized carbon and amorphous carbon [40].

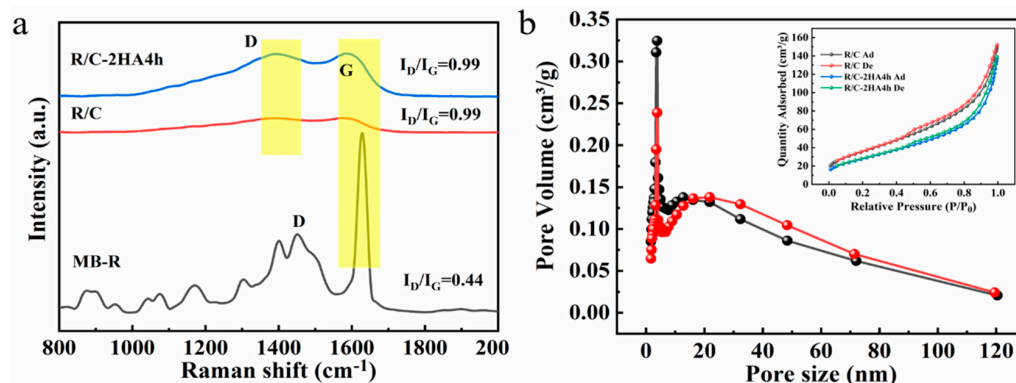


**Figure 3.** (a) Raman spectra of MB-R, R/C, and R/C-2HA4h; (b) the pore size distribution curves of R/C (black) and R/C-2HA4h (red) and N<sub>2</sub> adsorption–desorption isotherms of R/C and R/C-2HA4h (Inset).

### 3.3. BET Pore Structure Analysis

According to the IUPIC classification guideline, the R/C-2HA4h and R/C composites show type IIB isotherms with H<sub>3</sub> hysteresis ring (Figure 3b) [41,42]. At the relative pressure  $P/P_0 < 0.4$ , the adsorption–desorption curves almost coincided. When  $P/P_0 > 0.4$ , the capillary condensation phenomenon caused by multilayer adsorption of nitrogen can be seen, indicating mesopores, micropores, and/or macropores are present in the R/C and R/C-2HA4h composites [43]. The pore-diameter distribution curves of the composites are shown in Figure 3b. The peak of R/C and R/C-2HA4h is centered at 3.8 nm, revealing that the composite is a mesoporous material. The pore structure parameters of R/C and R/C-2HA4h were listed in Table S2 (Supplementary Material). The average pore size of R/C-2HA4h is higher than R/C, which is beneficial for R/C-2HA4h to adsorb BR and MB.

### 3.4. Influence of Adsorption Conditions

#### 3.4.1. Influence of Synthesis Parameters

The effects of the concentration of acid solution and the activation time on the adsorption capacity were investigated (see Figure 4). When the concentration of acid solution was 2 mol/L and the acid activation time was 4 h, the adsorption amount of the adsorbent to dye reached the best values (60.87 mg/g for MB; and 72.10 mg/g for BR). In Figure 4a, the adsorption amount of the acid-activated adsorbent for dyes is better than that without acid activation. Taking the composite adsorbents prepared under the optimal reaction conditions as the optimal adsorbent, the effect of pH, adsorption kinetics, adsorption isotherm and other adsorption behaviors of the adsorbent were investigated.

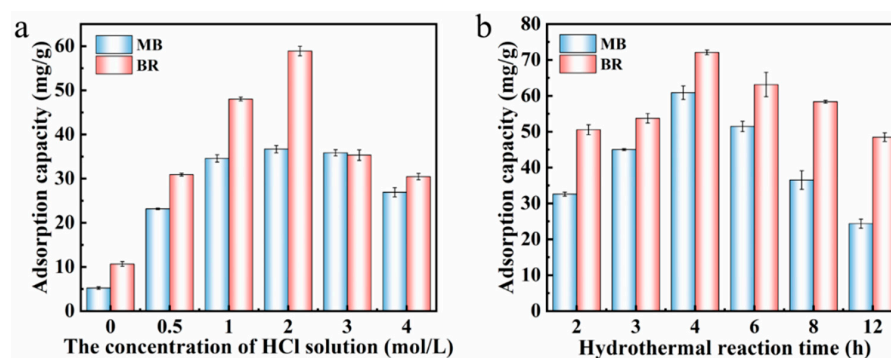


**Figure 4.** The effect of acid concentration (a) and activation time (b) on the adsorption amount of the as-prepared composites towards BR and MB dyes, respectively.

### 3.4.2. Effect of pH Values

The initial pH of the solution can affect the properties of dyes and the adsorbent, thus affect the adsorption behavior, especially for cationic dyes. As shown in Figure 5a,b, under each pH condition, the adsorption amount of R/C-2HA4h composite for dyes was much higher than that of R/C. In the test pH range (pH 2~10), the adsorption amount of R/C-2HA4h composite to BR is almost unaffected by the pH value, but it is slightly lower at pH 2~3, showing a very good pH immutability (Figure 5a). However, R/C-2HA4h composite is slightly pH-dependent for the adsorption of MB (Figure 5b). The adsorption capacity was relatively lower at pH 2~3, which increased rapidly with pH increasing from 2 to 4, and keeps almost constant at pH 4~10. The charge on R/C-2HA4h is negative (Figure 5c), which is conducive to the adsorption of positively charged cationic dyes. When pH is 2, because there are free  $H^+$  ions in the solution, some groups on the R/C-2HA4h change to  $Si-OH_2^+$ , which weaken the acting force between MB and the adsorbent, resulting in a slightly lower adsorption capacity towards MB [30]. When the pH value gradually increases to 6, the formed  $Si-OH_2^+$  also slowly change to  $Si-O^-$  groups, and more negative charges are on the adsorbent surface [44], so it is easy to adsorb positively charged MB. The removal rate ( $r$ ) of the adsorbents was compared with other adsorbents, as shown in Table 1. The  $r$  values of MB and BR of the R/C-2HA4h adsorbent were better than those of other adsorbents, which indicate that the adsorbent has better adsorption removal capability towards dyes.

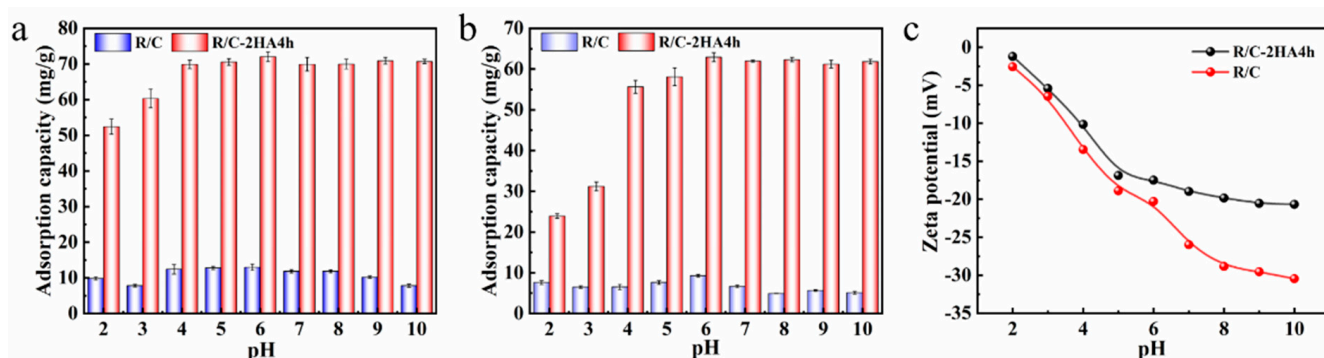


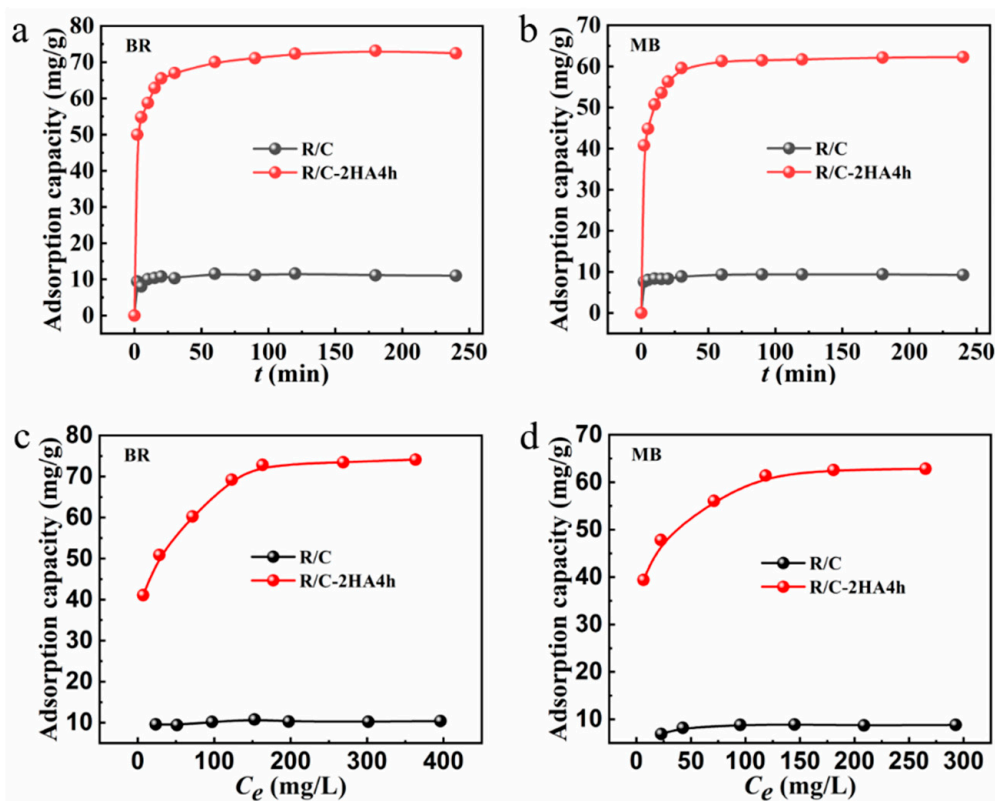
**Figure 5.** The adsorption capacity of the R/C and R/C-2HA4h composites (a) BR and (b) MB at variable pH; (c) Zeta potentials of the composite at variable pH.

**Table 1.** The comparison of removal rates ( $r$ ) of dyes using different adsorbents at the optimal pH.

Adsorbents	Dyes	Initial Concentration (mg/L)	$r$ (%) (optimal pH)	Ref.
F-CNTs@MOF@Gel	MB	100	81 (pH 7.89)	[45]
MnFe <sub>2</sub> O <sub>4</sub> /rGO	MB	100	95 (pH 7)	[46]
Tailing Ash	MB	20	96.2 (pH 10)	[47]
PpAP/Starch/GO	MB	100	96.7 (pH 7)	[48]
CNS/(PAAc-MAC)	MB	50	98 (pH 7)	[49]
Algal Biochar	MB	100	97.5 (pH 7)	[50]
Carbonized Dacryodes edulis leaf	MB	100	93 (pH 4)	[51]
R/C-2HA4h	MB	25	99.6 (pH 6)	This work
Valorization of olive-pomace	BR	200	90 (pH 7)	[52]
CuO nanoparticles	BR	10	80 (pH 7)	[53]
MCM-48	BR	500	97 (pH 4.6)	[54]
O-CM-chitosan hydrogel	BR	400	85 (pH 7)	[55]
Orange peel biochar	BR	100	94 (pH 10)	[56]
R/C-2HA4h	BR	25	99.5 (pH 6)	This work

### 3.4.3. Adsorption Kinetics and Isotherms

Figure 6a,b shows the time-dependent adsorption behavior of BR and MB by R/C-2HA4h and R/C composites. The variation in the adsorption rate is strongly correlated with the solid–liquid concentration gradient between the dye solution and the adsorbent. In the initial stage, due to the large concentration gradient, more adsorbates will diffuse onto the surface of the adsorbent, and at the same time, the adsorbent has more adsorption sites to trap dye molecules. When the time gradually increased, the adsorption amount also increased rapidly. With the gradual progress of the adsorption, the concentration gradient between solid and liquid becomes smaller, leading to a decrease of driving force for dye adsorption. Adsorption reaches equilibrium when all the adsorption sites were saturated [30]. The adsorption experiments of BR and MB by R/C-2HA4h adsorbent reached equilibrium within 30 min. Although R/C has poor adsorption capacity for BR and MB, the adsorption process reaches equilibrium rapidly (within 5 min). This may be because the fewer active adsorption sites on the surface of R/C can be rapidly occupied by dye molecules. When it is full, the adsorption reaches equilibrium immediately. As for adsorption kinetics, the experimental data were fitted using pseudo-first-order and pseudo-second-order kinetic models (Figure S4 in Supplementary Material) [57]. The fitting results with the pseudo-second-order model obtains a perfect linear relationship ( $R^2 > 0.99$ ), and the maximum adsorption amount calculated by the fitting is in agreement with the experimental value (Table S2 in Supplementary Material), which demonstrates that the kinetic adsorption behavior is consistent with the pseudo-second-order kinetic model, and chemisorption mainly contributes to the adsorption.



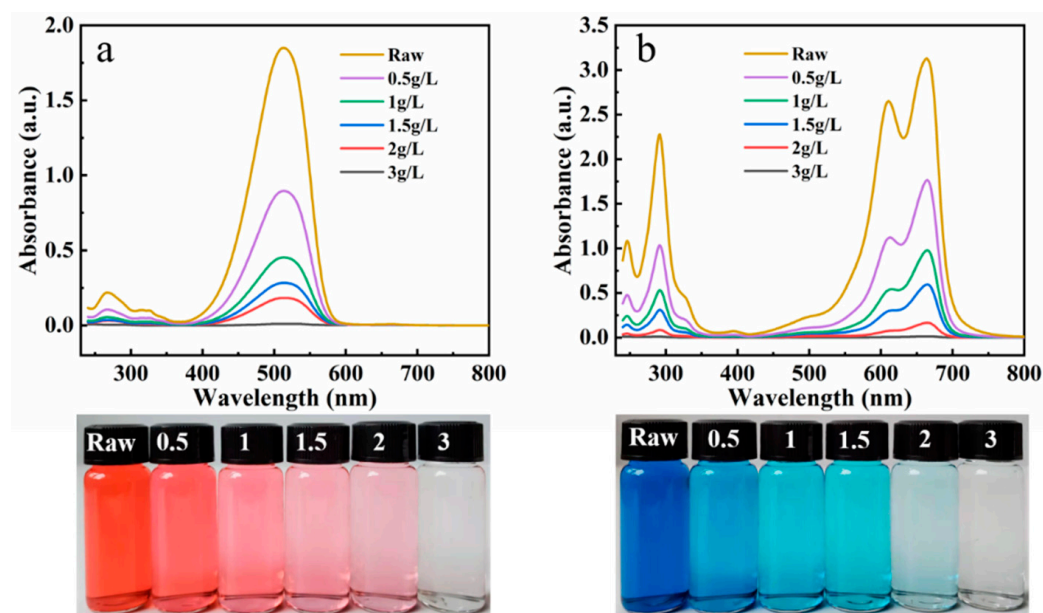
**Figure 6.** The change of adsorption amount of dye with altering adsorption time (a,b); The relationship curves of adsorption amount of BR and MB against the equilibrium concentration ( $C_e$ , mg/L) (c,d).

Figure 6c,d shows the variation curve of the adsorption capacity of dyes by the adsorbent with the equilibrium concentration of BR and MB after adsorption. In the initial stage, when the concentration of dye gradually increases, the adsorption amount also increases quickly. This is mainly because that the concentration gradient between

the adsorbent and the adsorbate gradually increase, and the dye molecules are more easily diffused onto the surface of the adsorbent [30]. The adsorption of BR onto R/C-2HA4h adsorbent reached equilibrium (adsorption capacity: 72.83 mg/g) at the initial BR concentration of 200 mg/L, and the adsorption of MB onto R/C-2HA4h reached equilibrium (adsorption capacity: 61.39 mg/g) at the initial MB concentration of 150 mg/g. Beyond this concentration, the available adsorption sites are almost saturated, the adsorption amount no longer increases with increasing dye concentration [58]. For adsorption isotherm, the experimental data were fitted using Langmuir isotherm model and Freundlich isotherm model (Figure S5 in Supplementary Material) [59]. The adsorption amounts calculated by Langmuir isotherm model were in good agreement with the experimental values (Table S3 in Supplementary Material), and the  $R^2$  of the Langmuir model are all above 0.99. The results show that the adsorption behavior is consistent with the Langmuir isotherm model, in which the adsorption process belongs to the monolayer adsorption.

#### 3.4.4. Removal Efficiency

The adsorption removal rate of MB and BR by the composite adsorbent was studied at the initial dye concentration of 25 mg/L and the variable adsorbent dosages (0.5, 1, 1.5, 2, and 3 g/L, respectively). After adsorption, the UV-Visible spectrum and digital photos of the solution were obtained (Figure 7a,b). The absorbance of the sample corresponding to the maximum absorption wavelength decreased with the increase in the amount of adsorbent, and the color of the solution became lighter. It is suggested that the removal rate can be improved by increasing the adsorbent dosage. When the adsorbent dosage was 3 g/L, both solutions (initial concentration: 25 mg/L) became colorless after adsorption (the removal rate of MB: 99.6%; the removal rate of BR: 99.5%), and the absorbance of the solution in the UV-Visible spectrum is almost zero. The adsorbent has a high removal rate for low-concentration dyes in solution, and has broad application prospects in the complete removal of dye effluent.



**Figure 7.** UV-Visible spectra and digital photos of the BR (a) and MB (b) solution before and after adsorption with different dose of R/C-2HA4h adsorbents.

#### 3.4.5. Single/Co-Adsorption in Real Water and Deionized Water

Due to the complexity of the actual water environment, the adsorption performance of the adsorbent in the actual water body is very important. The adsorption performance of the adsorbent towards MB and BR in three actual water samples (Yangtze River water, Yellow River water, and Seawater) were investigated (Figure 8). Encouragingly, the adsorption

performance of the composite adsorbent for both dyes in the actual water body is better, which may be due to the adsorbent having a stronger interaction with the dye molecules [60]. In addition, the adsorption property of the R/C-2HA4h adsorbent for MB and BR dyes in mixed solutions (MB or BR concentrations: 25 mg/L) were compared using three actual water samples and deionized water as solvent. As shown in Figure 8b–e, after adsorption with R/C-2HA4h adsorbent, when the amount of adsorbent increased gradually, the absorbance of the mixed dye solution decreased, and the color of the solution gradually changed light. In the three actual waters, when the dosage of the adsorbent was 3 g/L, the dye solution becomes colorless, and no absorbance peak was observed in the UV-Visible spectrum (the absorbance is almost 0) (Figure 8c–e). At this point, above 99.9% of the dye in the binary mixed solution was removed. In the deionized water (Figure 8b), the dye solution becomes colorless when the amount of the adsorbent was 5 g/L, and the dye in the binary mixed solution is completely removed at this time. For the adsorption of dyes in actual water, the dyes can be removed with a less amount of adsorbent. Therefore, the single/co-adsorption property of the composite material in real water and deionized water is better, which suggests its potential to be used for the removal and purification of multiple dyes in wastewater.

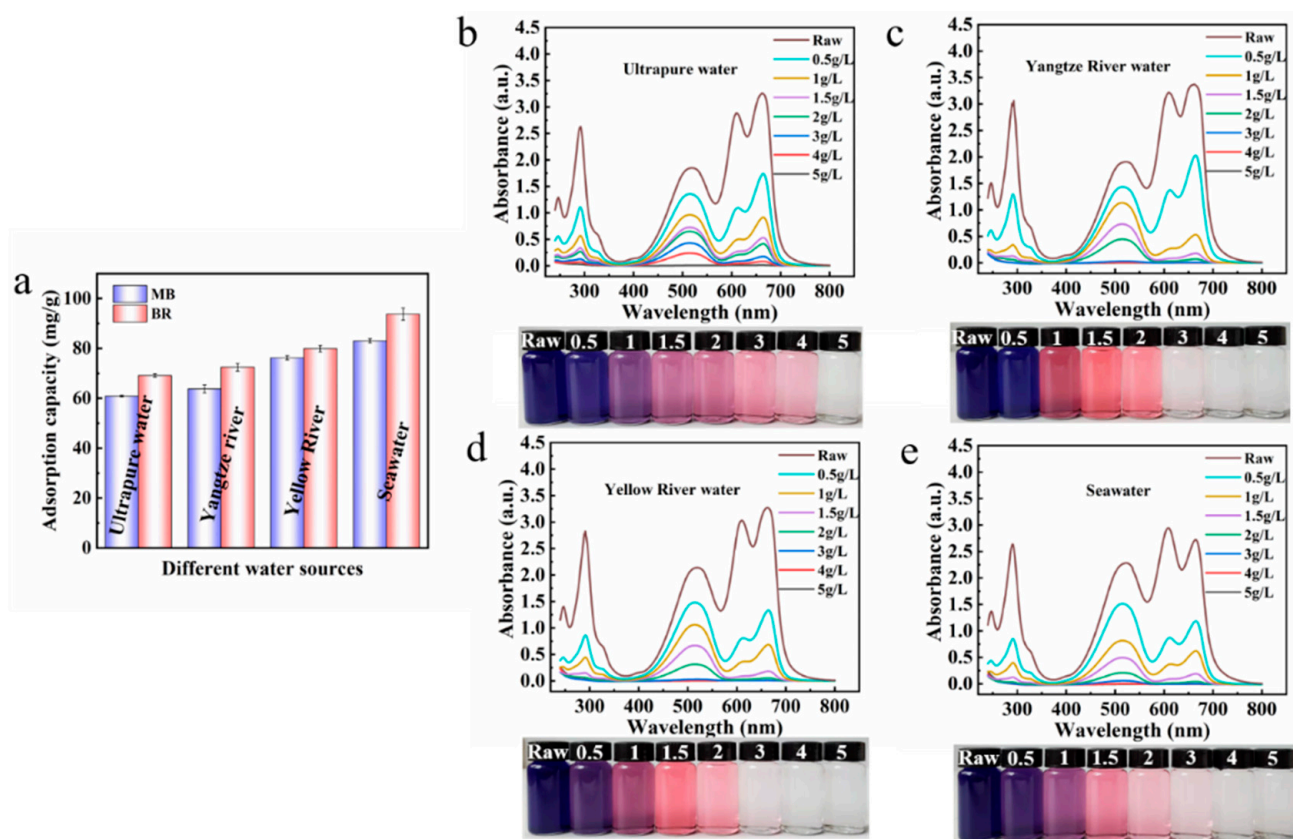


**Figure 8.** (a) The adsorption capacity of adsorbent for dyes in different water mediums (MB, 200 mg/L; BR, 200 mg/L; the dosage of adsorbent: 0.5 g/L). UV-Visible spectra of MB and BR mixed solution after adsorption with different dosages of R/C-2HA4h in deionized water (b), Yangtze River water (c), Yellow River water (d), and Seawater (e) (MB, 25 mg/L; BR, 25 mg/L). The illustrations are digital photos taken before and after adsorption of the binary mixed dye solution.

### 3.4.6. Reusability and Cost Analysis

After MB and BR dye solution (concentration: 400 mg/L) were adsorbed by the R/C-2HA4h adsorbent (1 g), the spent adsorbent can be regenerated via a calcination process at 400 °C followed by a washing process (Figure S1 in Supplementary Material). The adsorption-regeneration process is conducted five times, and the adsorption efficiency of

each regenerated adsorbent was tested to evaluate the reusability of the adsorbent. As shown in Figure S7 (Supplementary Material), after five regeneration–adsorption cycles, the adsorption efficiency of the adsorbent towards dyes can still reach more than 93%, which confirms that the adsorbent has good reusability.

Through a simple cost–benefit analysis, the practical application potential of the composite adsorbent was discussed. The cost analysis results of the composite adsorbent are shown in Table S5 (Supplementary Material). Since the main raw material for preparing the composite adsorbents is dye–clay waste, and clay has huge reserves in nature, the cost advantage of the adsorbent is obvious. The price of R/C-2HA4h composite adsorbent is about \$475/ton, which is far lower than the current average price of commercial activated carbon ( $\geq$ \$1200/ton). In addition, the composite adsorbent has more advantages in the removal of dyes in practical wastewater. Therefore, the composite adsorbent with good performance and economic benefits has a great potential for efficient purification of complex dye wastewater.

### 3.4.7. Adsorption Mechanism

The adsorption mechanism was studied by analyzing the dye-adsorbed adsorbent with XRD, FTIR spectra, BET, and XPS spectra. The diffraction peak of MB crystal is not seen in the XRD pattern of R/C-2HA4h-MB (Figure 9a), which shows that the MB dye is adsorbed on the adsorbent in a molecular form. It can be seen from the FTIR spectrum of R/C-2HA4h-MB (Figure 9b), after adsorption of MB, the new absorption bands appear at around 1602, 1489, 1390, and 1332  $\text{cm}^{-1}$  (the stretching vibration of aromatic C–C, the stretching vibration of aromatic C–N, and the antisymmetric and symmetric deformation bands of  $\text{CH}_3$  in MB, respectively) [30,36,37]. At 1630  $\text{cm}^{-1}$  (H–O–H bending), the absorption band of the adsorbent weakened slightly and shifted toward lower wavenumber region, demonstrating that there are hydrogen-bonding interactions between R/C-2HA4h and dyes. As shown in Table S2 (Supplementary Material), when the dye was adsorbed onto the adsorbent, the BET specific surface area decreased, indicating that dye molecules entered the pores. This also shows that the pore plays an important role in the adsorption of dye. The full-scan XPS spectra showed that the composition elements of R/C-2HA4h adsorbent are Si, Al, O, C, N, and Na (Figure 9c). After adsorbing the dye, the signal peaks of these elements all moved towards the low binding energy region, which was caused by the interaction of MB dye molecules with surface groups of rectorite during the adsorption process. The O 1s peak of R/C-2HA4h is divided into Si–OH, Si–O–Al, and Si–O–Si, which are located at 531.62, 532.18, and 532.56 eV, respectively [61], and they move to 531.33, 532.01, and 532.53 eV, respectively, after adsorption (Figure 9d). The Si 2p peak of R/C-2HA4h are divided Si–O–Al and Si–O–Si, which are located at 102.39 eV and 103.36 eV, respectively. After adsorption of MB, these peaks shift to 102.81 eV and 103.45 eV, respectively (Figure 9e). At the same time, the Al 2p peak of R/C-2HA4h and R/C-2HA4h-MB can be divided into two peaks, located at 74.68 eV (Si–O–Al) and 73.95 eV (Si–O–Al–O) and 74.16 (Si–O–Al) and 73.51 eV (Si–O–Al–O) (Figure 9f), respectively [62]. After adsorption of MB, the binding energy of these cleavage peaks shifts, and the peak area changes. This change is visible as aerobic groups are involved in the adsorption process of MB on R/C-2HA4h. In general, the main adsorption mechanisms of the composite adsorbents to dyes are electrostatic attraction, ion exchange, and hydrogen bond interaction between adsorbent and dye [63]. As for the adsorption of the composite adsorbent towards cationic dyes, the electrostatic attraction, ion exchange, hydrogen bonding, and chemical interaction between Si–O– group and dye group mainly contribute to the adsorption process (Figure 10). Therefore, the adsorbent has a good ability and potential to remove dyes.

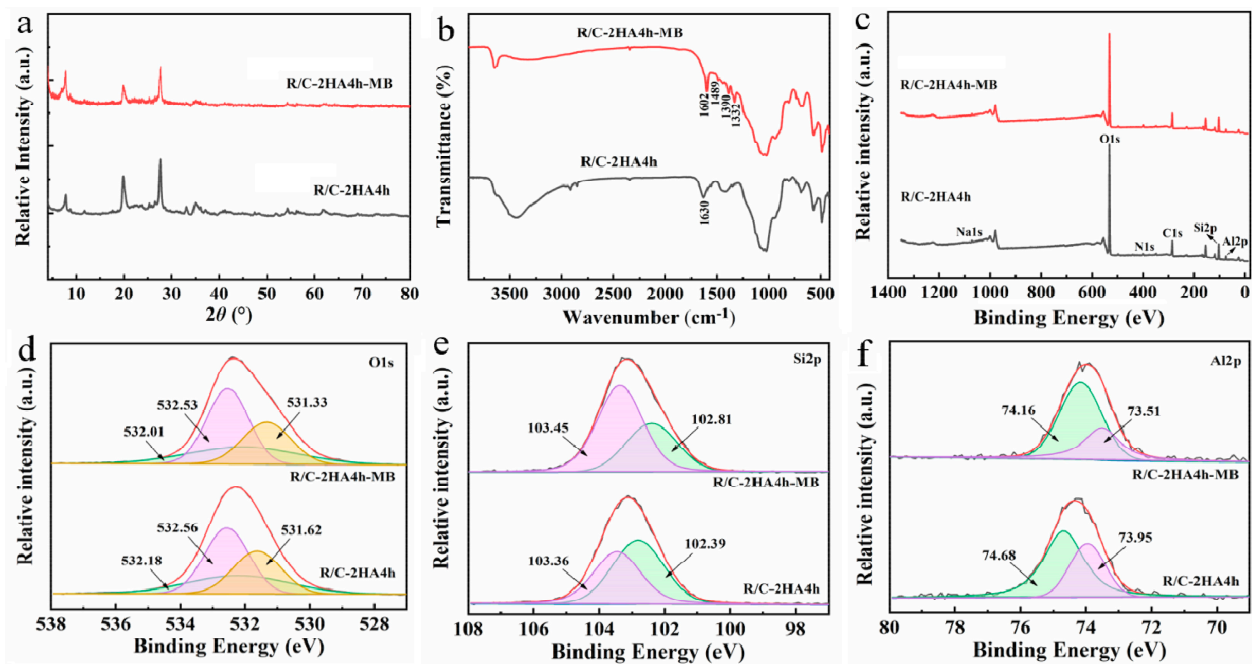


**Figure 9.** (a) XRD patterns of R/C-2HA4h and R/C-2HA4h-MB; (b) FTIR spectra of R/C-2HA4h and R/C-2HA4h-MB; Survey scanning XPS spectra of R/C-2HA4h and R/C-2HA4h-MB (c); and fine-scanning XPS spectra of O 1s (d), Si 2p (e), and Al 2p (f) of R/C-2HA4h and R/C-2HA4h-MB.

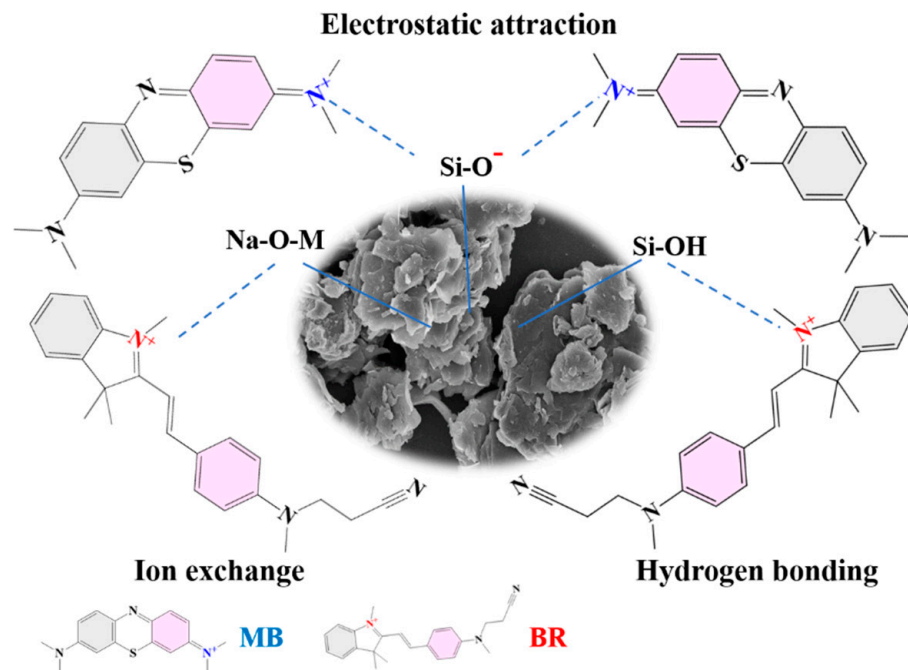


**Figure 10.** Interaction mechanism diagram of R/C-2HA4h adsorbent with MB and BR.

#### 4. Conclusions

Dye-loaded layered clay adsorbent waste was converted into a new carbon-in-silicate nanohybrid composite with ultrahigh removal ability for dyes at low concentrations. The dye intercalated in the interlayer spacing of rectorite can be converted into carbon sheet within the silicate, and the associated acid activation process can further create defects to produce more adsorption sites, which enable the resultant composite to completely remove dye in wastewater. Therefore, the composite adsorbent has a very high removal rate of 99.6% and 99.5% for MB and BR dyes (initial concentration: 25 mg/L), respectively.

The adsorption of dyes by the composite adsorbents conformed to the Langmuir isotherm model and the pseudo-second-order kinetic model, indicating that the adsorption process is a typical monolayer adsorption process, and chemisorption action is dominant. In addition, the composite adsorbent also shows high removal capacity for dyes in single-component and two-component solution system in deionized water and actual water (i.e., Yellow River water, Yangtze River water, and seawater) with a removal rate higher than 99%. The adsorbent has good reusability, and the adsorption efficiency is still above 93% after five regenerations. Moreover, the composite adsorbent is prepared from solid waste, so it has great potential for the purification of practical printing and dyeing wastewater.

**Supplementary Materials:** The following supporting information can be downloaded at: <https://www.mdpi.com/article/10.3390/nano13192627/s1>. Figure S1: Preparation diagram and regeneration cycle experiment diagram of R/C-2HA4h adsorbent; Figure S2: XRD patterns of R/C, and the composite adsorbents prepared at different concentration of acid solution (a) and acid activation time (b); FTIR spectra of R/C, and the composite adsorbents prepared at different concentration of acid solution (c) and activation time (d). Figure S3: The EDS image of (a) R/C and R/C-2HA4h(b). Figure S4: The plots of  $\log(q_e - q_t)$  versus  $t$  for the adsorption of BR (a) and MB (c) on the composite adsorbents (fitting with pseudo-first-order model); and the plots of  $t/q_t$  versus  $t$  for the adsorption of BR (c) and MB (d) on the composite adsorbents (fitting with pseudo-second-order model). Figure S5: The plots of  $C_e/q_e$  versus  $C_e$  for the adsorption of BR (a) and MB (c) on the composite adsorbents (fitting with Langmuir model); and the plots of  $\log q_e$  versus  $\log C_e$  for the adsorption of BR (b) and MB (d) on the composite adsorbents (fitting with Freundlich model). Figure S6:  $N_2$  adsorption-desorption isotherms of R/C-2HA4h and R/C-2HA4h-MB(a), the pore size distribution curves of R/C-2HA4h and R/C-2HA4h-MB (b). Figure S7: Recycling efficiency diagram of R/C-2HA4h. Table S1: pH and electrical conductivity of Yangtze River water, Yellow River water, Sea water. Table S2: Specific surface area and pore structure parameters for R/C, R/C-2HA4h, and R/C-2HA4h-MB. Table S3: Adsorption kinetic parameters calculated from the fitting results with pseudo-first-order and pseudo-second-order kinetic model for adsorption of BR and MB. Table S4: Adsorption isotherm parameters calculated from the fitting results of Langmuir and Freundlich model for adsorption of BR and MB. Table S5: Commercial cost—benefit analysis of composite adsorbents in dye wastewater purification in China. (see Refs. [64–67]).

**Author Contributions:** Conceptualization, W.W., F.G., Q.H. and J.Q.; Methodology, Q.H., F.G., J.Q., W.W. and X.L.; Validation, Q.H., X.L. and J.Q.; Formal Analysis, Q.H., J.Q. and H.Z.; Resources, Q.H., J.Q., H.Z. and X.L.; Data Curation, Q.H., J.Q., H.Z. and X.L.; Writing—Original Draft Preparation, Q.H., J.Q., H.Z. and X.L.; Writing—Review and Editing, W.W., F.G., Y.W. and X.L.; Validation, J.Q. and H.Z.; Visualization, Q.H., J.Q. and Y.W.; Supervision, W.W. and F.G.; Project Administration, W.W. and F.G.; Funding Acquisition, W.W. and F.G. All authors have read and agreed to the published version of the manuscript.

**Funding:** This research work was supported financially by the National Natural Science Foundation of China (No. 22068027), the Natural Science Foundation of Inner Mongolia (No. 2022MS05054), the Inner Mongolia Science Fund for Distinguished Young Scholars (2023JQ02), and the “Grassland Talents” Project of Inner Mongolia Autonomous Region (Grant No. CCYCLJ202).

**Data Availability Statement:** The data presented in this study are available upon request from the corresponding author.

**Conflicts of Interest:** The authors declare no conflict of interest.

## References

1. Postai, D.L.; Demarchi, C.A.; Zanatta, F.; Melo, D.C.C.; Rodrigues, C.A. Adsorption of rhodamine B and methylene blue dyes using waste of seeds of *Aleurites Moluccana*, a low cost adsorbent. *Alex. Eng. J.* **2016**, *55*, 1713–1723. [[CrossRef](#)]
2. Ibrahim, Y.; Meslam, M.; Eid, K.; Salah, B.; Abdullah, A.M.; Ozoemena, K.I.; Elzatahry, A.; Sharaf, M.A.; Sillanp, M. A review of MXenes as emergent materials for dye removal from wastewater. *Sep. Purif. Technol.* **2022**, *282*, 120083. [[CrossRef](#)]
3. Wang, Y.W.; Wang, W.B. Multifunctional materials with controllable super-wettability for oil-water separation and removal of pollutants: Design, emerging applications and challenges. *Carbon Neutralization* **2023**, *2*, 378–412. [[CrossRef](#)]

4. Motaghi, H.; Arabkhani, P.; Parvinnia, M.; Asfaram, A. Simultaneous adsorption of cobalt ions, azo dye, and imidacloprid pesticide on the magnetic chitosan/activated carbon@UiO-66 bio-nanocomposite: Optimization, mechanisms, regeneration, and application. *Sep. Purif. Technol.* **2022**, *284*, 120258. [[CrossRef](#)]
5. Qiu, B.B.; Shao, Q.N.; Shi, J.C.; Yang, C.H.; Chu, H.Q. Application of biochar for the adsorption of organic pollutants from wastewater: Modification strategies, mechanisms and challenges. *Sep. Purif. Technol.* **2022**, *300*, 121925. [[CrossRef](#)]
6. Sun, H.P.; Liu, Z.; Liu, X.Q.; Yu, C.L.; Wei, L.F. Preparation and characterization of Ppy/Bi<sub>2</sub>MoO<sub>6</sub> microspheres with highly photocatalytic performance for removal of highly concentrated organic dyes. *Mater. Today Sustain.* **2022**, *19*, 100154. [[CrossRef](#)]
7. Wang, X.; Zhang, H.; He, Q.D.; Xing, H.F.; Feng, K.; Guo, F.; Wang, W.W. Core-shell alginate beads as green reactor to synthesize grafted composite beads to efficiently boost single/co-adsorption of dyes and Pb(II). *Int. J. Biol. Macromol.* **2022**, *206*, 10–20. [[CrossRef](#)]
8. Tochetto, G.A.; De, O.D.; Hotza, D.; Immich, A.P.S.; Simao, L. Porous geopolymers as dye adsorbents: Review and perspectives. *J. Clean. Prod.* **2022**, *374*, 133982. [[CrossRef](#)]
9. Fang, K.; Deng, L.G.; Yin, J.Y.; Yang, T.H.; Li, J.B.; He, W. Recent advances in starch-based magnetic adsorbents for the removal of contaminants from wastewater: A review. *Int. J. Biol. Macromol.* **2022**, *218*, 909–929. [[CrossRef](#)]
10. Mandal, S.; Calderon, J.; Marpu, S.B.; Omary, M.A.; Shi, S.Q. Mesoporous activated carbon as a green adsorbent for the removal of heavy metals and Congo red: Characterization, adsorption kinetics, and isotherm studies. *J. Contam. Hydrol.* **2021**, *243*, 103869. [[CrossRef](#)]
11. Kumari, M.; Chaudhary, G.R.; Chaudhary, S.; Umar, A. Transformation of solid plastic waste to activated carbon fibres for wastewater treatment. *Chemosphere* **2022**, *294*, 133692. [[CrossRef](#)] [[PubMed](#)]
12. Ma, W.Y.; Liu, X.Y.; Lu, H.; He, Q.D.; Ding, K.; Wang, X.H.; Wang, W.B.; Guo, F. Chitosan-based composite hydrogel with a rigid-in-flexible network structure for pH-universal ultra-efficient removal of dye. *Int. J. Biol. Macromol.* **2023**, *241*, 124579. [[CrossRef](#)]
13. Njuguni, D.G.; Schnherr, S. Smart and regeneratable Xanthan gum hydrogel adsorbents for selective removal of cationic dyes. *J. Environ. Chem. Eng.* **2022**, *10*, 107620. [[CrossRef](#)]
14. Wan, X.X.; Rong, Z.H.; Zhu, K.X.; Wu, Y.M. Chitosan-based dual network composite hydrogel for efficient adsorption of methylene blue dye. *Int. J. Biol. Macromol.* **2022**, *222 Pt A*, 725–735. [[CrossRef](#)]
15. Wang, W.B.; Tian, G.Y.; Zhang, Z.F.; Wang, A.Q. A simple hydrothermal approach to modify palygorskite for high-efficient adsorption of Methylene blue and Cu(II) ions. *Chem. Eng. J.* **2015**, *265*, 228–238. [[CrossRef](#)]
16. Joshi, P.; Raturi, A.; Srivastava, M.; Khatri, O.P. Graphene oxide, kaolinite clay and PVA-derived nanocomposite aerogel as a regenerative adsorbent for wastewater treatment applications. *J. Environ. Chem. Eng.* **2022**, *10*, 108597. [[CrossRef](#)]
17. Mukherjee, D.; Das, P.; Prasad, G.N.; Katha, A.R.; Gumma, S.; Mandal, B. Hierarchical graphite oxide decorated UiO-66 for ultrahigh adsorption of dye with synergistic effect of ultrasonication: Experimental and density functional theory study. *Sep. Purif. Technol.* **2022**, *294*, 121217. [[CrossRef](#)]
18. Wang, F.; Li, L.; Iqbal, J.; Yang, Z.R.; Du, Y.P. Preparation of magnetic chitosan corn straw biochar and its application in adsorption of amaranth dye in aqueous solution. *Int. J. Biol. Macromol.* **2022**, *199*, 234–242. [[CrossRef](#)]
19. Shu, Q.; Qiu, W.; Luo, M.; Xiao, L. Morphology-controlled hydrothermal synthesis of copper selenides with orange juice for highly efficient cationic dyes adsorption. *Mater. Today Sustain.* **2022**, *17*, 100094. [[CrossRef](#)]
20. Dai, X.J.; Yi, W.; Yin, C.Q.; Li, K.L.; Feng, L.; Zhou, Q.; Yi, Z.Y.; Zhang, X.B.; Wang, Y.L.; Yu, Y.L.; et al. 2D-3D magnetic NiFe layered double hydroxide decorated diatomite as multi-function material for anionic, cationic dyes, arsenate, and arsenite adsorption. *Appl. Clay Sci.* **2022**, *229*, 106664. [[CrossRef](#)]
21. Kumar, A.S.K.; Warchol, J.; Matusik, J.; Tseng, W.L.; Bajda, N.R.T. Heavy metal and organic dye removal via a hybrid porous hexagonal boron nitride-based magnetic aerogel. *NPJ Clean Water* **2022**, *5*, 24. [[CrossRef](#)]
22. Ewis, D.; M.Ba-Abbad, M.; Benamor, A.; H.El-Naas, M. Adsorption of organic water pollutants by clays and clay minerals composites: A comprehensive review. *Appl. Clay Sci.* **2022**, *229*, 106686. [[CrossRef](#)]
23. Lan, D.W.; Zhu, H.W.; Zhang, J.W.; Li, S.; Chen, Q.H.; Wang, C.X.; Wu, T.; Xu, M.X. Adsorptive removal of organic dyes via porous materials for wastewater treatment in recent decades: A review on species, mechanisms and perspectives. *Chemosphere* **2022**, *293*, 133464.
24. Wu, X.P.; Xu, Y.Q.; Zhang, X.L.; Wu, Y.C.; Gao, P. Adsorption of low-concentration methylene blue onto a palygorskite/carbon composite. *New Carbon Mater.* **2015**, *30*, 71–78. [[CrossRef](#)]
25. Zhang, H.; He, Q.D.; Zhao, W.T.; Guo, F.; Han, L.; Wang, W.B. Superior dyes removal by a recyclable magnetic silicate@Fe<sub>3</sub>O<sub>4</sub> adsorbent synthesized from abundant natural mixed clay. *Chem. Eng. Res. Des.* **2021**, *175*, 272–282. [[CrossRef](#)]
26. Zhao, Q.H.; Yin, W.W.; Long, C.H.; Jiang, Z.Y.; Jiang, J.L.; Yang, H.M. Insights into the adsorption behaviour and mechanism of tetracycline on rectorite mineral: Influence of surface and structure evolution. *Appl. Clay Sci.* **2022**, *229*, 106698. [[CrossRef](#)]
27. Xie, W.M.; Wang, J.; Fu, L.J.; Tan, Q.; Tan, X.M.; Yang, H.M. Evolution of the crystallographic structure and physicochemical aspects of rectorite upon calcination. *Appl. Clay Sci.* **2019**, *185*, 105374. [[CrossRef](#)]
28. Chen, H.Y.; Lu, C.; Yang, H.M. Lanthanum compounds-modified rectorite composites for highly efficient phosphate removal from wastewater. *Appl. Clay Sci.* **2020**, *199*, 105875.
29. Zhu, R.L.; Chen, Q.Z.; Wang, X.; Wang, S.Y.; Zhu, J.X.; He, H.P. Templated synthesis of nitrogen-doped graphene-like carbon materials using spent montmorillonite. *RSC Adv.* **2015**, *5*, 7522–7528. [[CrossRef](#)]

30. Wang, W.B.; Lu, T.T.; Chen, Y.L.; Tian, G.Y.; Sharma, V.K.; Zhu, Y.F.; Zong, L.; Wang, A.Q. Mesoporous silicate/carbon composites derived from dye-loaded palygorskite clay waste for efficient removal of organic contaminants. *Sci. Total Environ.* **2019**, *696*, 133955. [[CrossRef](#)]
31. Tian, G.Y.; Wang, W.B.; Zong, L.; Kang, Y.R.; Wang, A.Q. From spent dye-loaded palygorskite to a multifunctional palygorskite/carbon/Ag nanocomposite. *RSC Adv.* **2016**, *6*, 41696–41706. [[CrossRef](#)]
32. Zhai, P.X.; Liu, H.B.; Sun, F.W.; Chen, T.H.; Zou, X.H.; Wang, H.L.; Chu, Z.Y.; Wang, C.; Liu, M.; Chen, D. Carbonization of methylene blue adsorbed on palygorskite for activating peroxydisulfate to degrade bisphenol A: An electron transfer mechanism. *Appl. Clay Sci.* **2022**, *216*, 106327. [[CrossRef](#)]
33. Tian, C.S.; Rao, Y.Z.; Su, G.; Huang, T.; Xiang, C.R. The Thermal Decomposition Behavior of Pyrite-Pyrrhotite Mixtures in Nitrogen Atmosphere. *J. Chem.* **2022**, *2022*, 1–11. [[CrossRef](#)]
34. Chen, Q.Z.; Liu, H.M.; Zhu, R.L.; Wang, X.; Wang, S.Y.; Zhu, J.X.; He, H.P. Facile synthesis of nitrogen and sulfur co-doped graphene-like carbon materials using methyl blue/montmorillonite composites. *Microporous Mesoporous Mater.* **2016**, *225*, 137–143. [[CrossRef](#)]
35. Chen, H.; Zhao, Y.G.; Wang, A.Q. Removal of Cu(II) from aqueous solution by adsorption onto acid-activated palygorskite. *J. Hazard. Mater.* **2007**, *149*, 346–354.
36. Li, Z.H.; Chang, P.H.; Jiang, W.T.; Jean, J.S.; Hong, H.L. Mechanism of methylene blue removal from water by swelling clays. *Chem. Eng. J.* **2011**, *168*, 1193–1200. [[CrossRef](#)]
37. Xiong, L.; Yang, Y.; Mai, J.X.; Zhang, C.Y.; Wei, D.P.; Chen, Q.; Ni, J. Adsorption behavior of methylene blue onto titanate nanotubes. *Chem. Eng. J.* **2010**, *156*, 313–320. [[CrossRef](#)]
38. Regmi, P.; Moscoso, J.L.G.; Kumar, S.; Cao, X.Y.; Mao, J.D.; Schafran, G. Removal of copper and cadmium from aqueous solution using switchgrass biochar produced via hydrothermal carbonization process. *J. Environ. Manag.* **2012**, *109*, 61–69. [[CrossRef](#)]
39. Ruiz-Hitzky, E.; Darder, M.; Fernandes, F.M.; Zatile, E.; Palomares, F.J.; Aranda, P. Supported graphene from natural resources: Easy preparation and applications. *Adv. Mater.* **2011**, *23*, 5250–5255. [[CrossRef](#)]
40. Zhou, X.; Wang, P.L.; Zhang, Y.G.; Wang, L.L.; Zhang, L.T.; Zhang, L.; Xu, L.; Liu, L. Biomass based nitrogen-doped structure-tunable versatile porous carbon materials. *J. Mater. Chem. A* **2017**, *5*, 12958–12968. [[CrossRef](#)]
41. Li, T.; Shen, J.F.; Huang, S.T.; Li, N.; Ye, M.X. Hydrothermal carbonization synthesis of a novel montmorillonite supported carbon nanosphere adsorbent for removal of Cr(VI) from waste water. *Appl. Clay Sci.* **2014**, *93–94*, 48–55. [[CrossRef](#)]
42. Sing, K.S.W. Reporting physisorption data for gas/solid systems with special reference to the determination of surface area and porosity (Provisional). *Pure Appl. Chem.* **1985**, *57*, 603–619. [[CrossRef](#)]
43. Kumar, A.S.K.; Kalidhasan, S.; Rajesh, V.; Rajesh, N. A meticulous study on the adsorption of mercury as tetrachloromercurate (II) anion with trioctylamine modified sodium montmorillonite and its application to a coal fly ash sample. *Ind. Eng. Chem. Res.* **2012**, *51*, 11312–11327. [[CrossRef](#)]
44. Potgieter, J.H.; Potgieter-Vermaak, S.S.; Kalibantonga, P.D. Heavy metals removal from solution by palygorskite clay. *Miner. Eng.* **2006**, *19*, 463–470. [[CrossRef](#)]
45. Zhang, Y.; Li, Y.H.; Wang, M.Z.; Chen, B.; Sun, Y.H.; Chen, K.W.; Du, Q.J.; Pi, X.X.; Wang, Y.Q. Adsorption of Methylene Blue from Aqueous Solution Using Gelatin-Based Carboxylic Acid-Functionalized Carbon Nanotubes@Metal–Organic Framework Composite Beads. *Nanomaterials* **2022**, *12*, 2533. [[CrossRef](#)] [[PubMed](#)]
46. Adel, M.; Ahmed, M.A.; Mohamed, A.A. A facile and rapid removal of cationic dyes using hierarchically porous reduced graphene oxide decorated with manganese ferrite. *FlatChem* **2021**, *26*, 100233. [[CrossRef](#)]
47. Yahya, C.J.F.B.; Choong, T.S.Y.; Li, F.; Ghani, W.A.W.A.K.; Aziz, F.N.A.A.; Jamil, S.N.A.M. Tailing Ash for the Removal of Methylene Blue from Aqueous Solutions by Batch Adsorption. *Processes* **2023**, *11*, 2282. [[CrossRef](#)]
48. Iamail, H.K.; Ali, L.I.A.; Alesary, H.F.; Nile, B.K.; Barton, S. Synthesis of a poly(p-aminophenol)/starch/graphene oxide ternary nanocomposite for removal of methylene blue dye from aqueous solution. *J. Polym. Res.* **2022**, *29*, 1–22.
49. Tang, Z.Q.; Hu, X.S.; Ding, H.Y.; Li, Z.J.; Liang, R.; Sun, G.X. Villi-like poly(acrylic acid) based hydrogel adsorbent with fast and highly efficient methylene blue removing ability. *J. Colloid Interface Sci.* **2021**, *594*, 54–63. [[CrossRef](#)]
50. Xu, J.; Fu, M.Y.; Ma, Q.H.; Zhang, X.P.; You, C.H.; Shi, Z.F.; Lin, Q.; Wang, X.H.; Feng, W. Modification of biochar by phosphoric acid via wet pyrolysis and using it for adsorption of methylene blue. *RSC Adv.* **2023**, *13*, 15327–15333. [[CrossRef](#)]
51. Nnaji, N.J.N.; Sonde, C.U.; Nwanji, O.L.; Ezech, G.C.; Onuigbo, A.U.; Ojukwu, A.M.; Mbah, P.C.; Adewumi, A.O.; Unoka, E.C.; Otedo, J.O.; et al. Dacryodes edulis leaf derived biochar for methylene blue biosorption. *J. Environ. Chem. Eng.* **2023**, *11*, 109638. [[CrossRef](#)]
52. Graba, Z.; Akkari, I.; Bezzi, N.; Kaci, M.M. Valorization of olive-pomace as a green sorbent to remove Basic Red 46 (BR46) dye from aqueous solution. *Biomass Convers. Biorefinery* **2022**. [[CrossRef](#)]
53. Asl, M.N.; Mahmodi, N.M.; Teymouri, P.; Shahmoradi, B.; Rezaee, R.; Maleki, A. Adsorption of organic dyes using copper oxide nanoparticles: Isotherm and kinetic studies. *Desalination Water Treat.* **2016**, *57*, 25278–25287.
54. Gucbilmez, Y.; Yavuz, Y.; Calis, I.; Yargic, A.S.; Koparal, A.S. Low temperature synthesis of MCM-48 and its adsorbent capacity for the removal of basic red 29 dye from model solutions. *Helvion* **2023**, *9*, 15659.
55. Al-Harby, N.F.; Almutairi, R.S.; Elmehbad, N.Y.; Mohamed, N.A. A novel O-carboxymethyl chitosan-based hydrogel of an outstanding adsorption performance for removal of cationic Basic Red 12 dye from its aqueous solution. *Polym. Eng. Sci.* **2023**, *63*, 2336–2353. [[CrossRef](#)]

56. Kapoor, D.R.T.; Sivamani, D.S. Adsorptive Potential of Orange Peel Biochar for Removal of Basic Red 46 Dye and Phytotoxicity Analysis. *Chem. Eng. Technol.* **2023**, *46*, 756–765. [[CrossRef](#)]
57. Cai, Y.H.; Tang, B.; Bin, L.Y.; Huang, S.S.; Li, P.; Fu, F.L. Constructing a multi-layer adsorbent for controllably selective adsorption of various ionic dyes from aqueous solution by simply adjusting pH. *Chem. Eng. J.* **2020**, *382*, 122829. [[CrossRef](#)]
58. Li, H.J.; Miao, L.; Zhao, G.Q.; Jia, W.Z.; Zhu, Z.R. Preparation of high-performance chitosan adsorbent by cross-linking for adsorption of Reactive Red 2 (RR2) dye wastewater. *J. Environ. Chem. Eng.* **2022**, *10*, 108872. [[CrossRef](#)]
59. Cai, K.; Shen, W.; Ren, B.Y.; He, J.; Wu, S.Z.; Wang, W. A Phytic acid modified CoFe<sub>2</sub>O<sub>4</sub> magnetic adsorbent with controllable morphology, excellent selective adsorption for dyes and ultra-strong adsorption ability for metal ions. *J. Environ. Chem. Eng. J.* **2017**, *330*, 936–946. [[CrossRef](#)]
60. Shi, J.D.; Guo, C.; Lei, C.Y.; Liu, Y.Y.; Hou, X.H.; Zheng, X.; Hu, Q. High-performance biochar derived from the residue of Chaga mushroom (*Inonotus obliquus*) for pollutants removal. *Bioresour. Technol.* **2022**, *344*, 126268. [[CrossRef](#)] [[PubMed](#)]
61. Hsiao, M.C.; Ma, C.C.M.; Chiang, J.C.; Ho, K.K.; Chou, T.Y.; Xie, X.F.; Tsai, C.H.; Chang, L.H.; Hsieh, C.K. Thermally conductive and electrically insulating epoxy nanocomposites with thermally reduced graphene oxide-silica hybrid nanosheets. *Nanoscale* **2013**, *5*, 5863–5871. [[CrossRef](#)]
62. Wang, W.B.; Zhao, W.T.; Zhang, H.; Xu, J.; Zong, L.; Kang, Y.R.; Wang, A.Q. Mesoporous polymetallic silicate derived from naturally abundant mixed clay: A potential robust adsorbent for removal of cationic dye and antibiotic. *Powder Technol.* **2021**, *390*, 303–314. [[CrossRef](#)]
63. Shi, Y.W.; Chang, Q.T.; Zhang, W.; Song, G.B.; Sun, Y.; Ding, G.H. A review on selective dye adsorption by different mechanisms. *J. Environ. Chem. Eng.* **2022**, *10*, 108639. [[CrossRef](#)]
64. Langmuir, I. The Constitution and fundamental properties of solids and liquids. II. liquids. *J. Am. Chem. Soc.* **1916**, *39*, 1848–1906. [[CrossRef](#)]
65. Freundlich, H. Over the adsorption in solution. *J. Phys. Chem.* **1906**, *57*, 1100–1107.
66. Ho, Y.S. A review of potentially low cost adsorbent for heavy metals. *Scientometrics* **2004**, *59*, 171–177.
67. Ho, Y.S.; Fellow, M.K. A Comparison of Chemisorption Kinetic Models Applied to Pollutant Removal on Various Sorbents. *Process Saf. Environ. Prot.* **1998**, *76*, 332–340. [[CrossRef](#)]

**Disclaimer/Publisher's Note:** The statements, opinions and data contained in all publications are solely those of the individual author(s) and contributor(s) and not of MDPI and/or the editor(s). MDPI and/or the editor(s) disclaim responsibility for any injury to people or property resulting from any ideas, methods, instructions or products referred to in the content.